
REOBench: Benchmarking Robustness of Earth Observation Foundation Models

Xiang Li^{1*}, Yong Tao^{2*}, Siyuan Zhang^{3*}, Siwei Liu⁴, Zhitong Xiong⁵
Chunbo Luo², Lu Liu², Mykola Pechenizkiy⁶, Xiao Xiang Zhu⁵, Tianjin Huang^{2,6}

¹ University of Reading, UK ² University of Exeter, UK ³ South China Normal University, China

⁴ Mohamed bin Zayed University of Artificial Intelligence, United Arab Emirates

⁵ Technical University of Munich, Germany ⁶ Eindhoven University of Technology, NL

Abstract

Earth observation foundation models have shown strong generalization across multiple Earth observation tasks, but their robustness under real-world perturbations remains underexplored. To bridge this gap, we introduce REOBench, the first comprehensive benchmark for evaluating the robustness of Earth observation foundation models across six tasks and twelve types of image corruptions, including both appearance-based and geometric perturbations. To ensure realistic and fine-grained evaluation, our benchmark focuses on high-resolution optical remote sensing images, which are widely used in critical applications such as urban planning and disaster response. We conduct a systematic evaluation of a broad range of models trained using masked image modeling, contrastive learning, and vision-language pre-training paradigms. Our results reveal that ❶ existing Earth observation foundation models experience significant performance degradation when exposed to input corruptions. ❷ The severity of degradation varies across tasks, model architectures, backbone sizes, and types of corruption, with performance drop varying from less than 1% to over 20%. ❸ Vision-language models show enhanced robustness, particularly in multimodal tasks. REOBench underscores the vulnerability of current Earth observation foundation models to real-world corruptions and provides actionable insights for developing more robust and reliable models. Code and data are publicly available at <https://github.com/lx709/REOBench>.

1 Introduction

Recent studies have shown that foundation models pre-trained on large-scale datasets have demonstrated powerful capabilities across multiple domains. Models such as MAE [1], CLIP [2], MiniGPT-4 [3], and LLaVA [4] have achieved remarkable success in multiple vision and vision-language tasks. These models are capable of extracting representative features from images, and more importantly, can be quickly adapted to multiple downstream tasks with minimal fine-tuning, significantly improving the efficiency and effectiveness of task-solving.

In the field of remote sensing, the rapid growth in data volume has sparked significant interest in developing foundation models for remote sensing image analysis. Earth observation foundation models (EOFMs) aim to leverage supervised or self-supervised training to build large-scale pre-trained models that can be adapted to a wide range of downstream tasks, thereby improving the performance and efficiency of Earth observation applications. In recent years, a growing body of research has focused on constructing such foundation models tailored for remote sensing. Mainstream models can be divided into unimodal pre-trained foundation models (e.g., SatMAE [5], RingMo [6],

*First three authors contributed equally.

ScaleMAE [7], SpectralGPT [8]) and vision-language foundation models (e.g., RemoteCLIP [9], GeoRSClip [10], RSGPT [11], GeoChat [12]). These EOFMs have demonstrated their powerful performance in numerous downstream tasks. A comprehensive review of EOFMs can be found in [13–19].

Despite advancements in EOFMs, there remains a significant gap in systematically benchmarking their robustness towards image perturbations. Remote sensing images are particularly susceptible to factors such as weather conditions or sensor discrepancies, which can introduce significant noise and variability [20–22], posing challenges to current EOFMs. Therefore, developing a comprehensive benchmark to evaluate and compare the robustness of these models holds great academic and practical significance. Such benchmarking efforts can guide the design of highly robust EOFMs that effectively adapt to noise and data variability, ensuring stable and reliable results under diverse conditions.

To achieve this, we introduce **REOBench**, a comprehensive **Benchmark** designed to evaluate the **Robustness of Earth Observation** foundation models, covering state-of-the-art models based on masked image modeling, contrastive learning, and large language models. REOBench focuses on **high-resolution optical remote sensing images**, which are widely used in real-world applications such as urban planning and disaster response. We conducted experiments on **six** widely studied remote sensing image understanding tasks, covering both vision-centric and vision-language tasks, under **twelve** types of perturbations. These include both appearance-based corruptions (e.g., noise, blur, haze) and geometric distortions (e.g., rotation, scale, translation), applied at varying severity levels to simulate realistic environmental and sensor-induced challenges. Our evaluation yields three key findings:

- ★ Existing Earth observation foundation models suffer noticeable performance degradation under common image corruptions, with particularly sharp drops for the models based on masked image modeling.
- ★ The degree of vulnerability to image corruptions varies across tasks, model architectures, and types of perturbations, with performance drop varying from less than 1% to over 20%.
- ★ Vision-language foundation models exhibit greater robustness to visual perturbations compared to vision-centric foundation models, particularly in image-level scene classification tasks.

In summary, REOBench provides the first large-scale, task-diverse, and perturbation-rich benchmark for evaluating robustness in EOFMs. It offers actionable insights for the research community and serves as a stepping stone toward building more reliable, generalizable, and trustworthy AI systems for Earth observation.

2 REOBench Dataset

To systematically evaluate the robustness of EOFMs, we construct a benchmark dataset by incorporating widely used remote sensing datasets spanning diverse tasks. Specifically, we include AID [23] for scene classification, ISPRS Potsdam [24] for semantic segmentation, DIOR [25] for object detection, and three subsets from VRSBench [26] for image captioning, visual question answering (VQA), and visual grounding. These datasets are selected based on their popularity, diversity of content, and relevance to the tasks under evaluation.

2.1 Corruptions in Remote Sensing Images

Remote sensing platforms are subject to a wide range of visual degradations that differ significantly from those encountered by ground-based cameras. To systematically evaluate the robustness of RSFMs, we construct a benchmark comprising **12 synthetic corruptions**, categorized into three types: *environmental*, *sensor-induced*, and *geometric*. Each corruption is generated using physically or statistically grounded procedures to ensure the resulting images remain photorealistic while faithfully reflecting failure modes commonly observed in satellite and UAV imagery.

Environmental Corruptions. Atmospheric and illumination variations constitute predominant environmental degradations. For instance, *Cloud* occlusions substantially obscure optical remote sensing data, severely impacting scene interpretability [27, 28]. Variations in *Brightness* resulting from shifting sun angles affect radiometric stability and degrade feature matching and object recognition performance [29, 30]. *Haze*, caused by aerosol scattering, significantly lowers image contrast and

impairs detection and classification accuracy [31, 32]. Following established benchmarks [33], we simulate these environmental corruptions using physically motivated image augmentation techniques.

Sensor-induced Corruptions. Imperfections during sensor capture or data transmission introduce various degradations. *Gaussian Blur*, indicative of defocusing or modulation transfer function (MTF) degradation, compromises tie-point accuracy and feature localization [34, 35]. *Motion Blur*, arising from platform vibrations or rapid movements, negatively impacts object detection and tracking in aerial inspections [36]. *Gaussian Noise* and *Salt & Pepper Noise*, simulating electronic interference and bit-flip errors respectively, significantly decrease segmentation and classification accuracy [37, 38]. *Sensor Gap* degradations, exemplified by the Landsat-7 SLC-off issue, necessitate specialized gap-filling methodologies [39, 40]. Furthermore, *Compression* artifacts, such as those from JPEG/JPEG2000, substantially impair the quality of CNN feature extraction [41]. These sensor-induced corruptions are replicated through established augmentation and simulation protocols in line with existing research [33, 42].

Geometric Corruptions. Geometric distortions originate primarily from variations in sensor orientation, altitude, and registration accuracy. *Rotation* caused by platform roll or yaw introduces inconsistencies in orientation-sensitive feature extraction processes [43]. *Scale* alterations resulting from altitude fluctuations pose significant challenges for detectors lacking robust multi-scale adaptability [44]. *Translation*, modeling inaccuracies due to GPS drift, registration errors, or parallax, adversely affects pixel-aligned or patch-based analysis methods [45]. To effectively simulate these geometric degradations, we apply spatial transformations, including image *Rotation*, *Scaling*, and *Translation*, to remote sensing images.

In total, these corruption categories encompass twelve distinct types. Each type of corruption is applied consistently across all datasets at five severity levels. Fig. 1 illustrates one example of original and corrupted images.

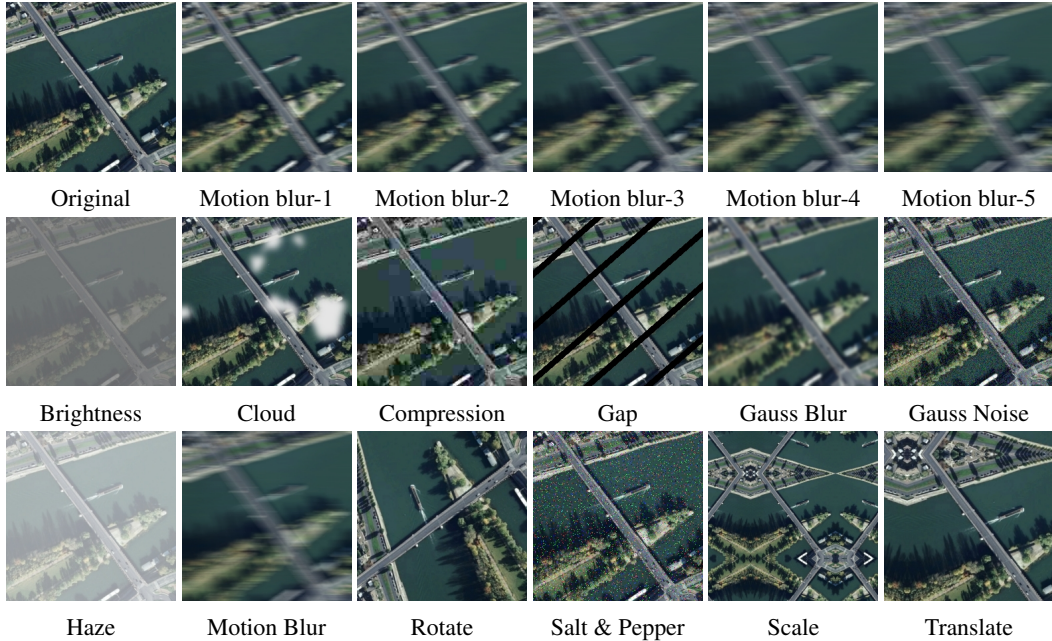


Figure 1: Example of perturbed images. In the first row, we present the original clean image alongside images perturbed by five levels of motion blur. The second and third rows illustrate examples of images corrupted by a range of perturbation types.

2.2 Definition of Corruption Robustness

We formalize the corruption robustness of EOFMs as its ability to maintain task performance in the presence of realistic geophysical and sensor-induced degradations frequently encountered in Earth observation. Let $f : \mathcal{X} \rightarrow \mathcal{Y}$ denote an EOFMs that maps an input image $x \in \mathcal{X}$ to a label $y \in \mathcal{Y}$,

with (x, y) sampled from an underlying geospatial data-generating distribution \mathcal{D} . We define a set of corruptions $\mathcal{C} = \{c_1, \dots, c_K\}$, where each $c_k \in \mathcal{C}$ represents a physically plausible corruption operator, such as haze, cloud occlusion, or sensor noise. Each corruption occurs with a non-zero prevalence $\mathbb{P}_{\mathcal{C}}(c_k) > 0$. To quantify robustness, we introduce the *task performance drop* Δ_{TP} , which captures the expected degradation in performance when the model is evaluated on corrupted inputs:

$$\Delta_{\text{TP}} = \mathbb{P}_{(x,y) \sim \mathcal{D}}[f(x) = y] - \mathbb{E}_{c \sim \mathcal{C}}[\mathbb{P}_{(x,y) \sim \mathcal{D}}[f(c(x)) = y]]. \quad (1)$$

A *smaller* Δ_{TP} value indicates *greater* robustness, as it reflects a smaller degradation in performance when the model encounters realistic corruptions.

3 Benchmark Robustness on EOFMs

We evaluate the robustness of EOFMs across six widely studied remote sensing image understanding tasks: scene classification, semantic segmentation, object detection, image captioning, visual question answering (VQA), and visual grounding. The evaluated models represent the current state-of-the-art in remote sensing and can be broadly categorized into the following three types.

MIM-based foundation models. Masked image modeling (MIM) has gained popularity through the pioneering work of MAE [1]. In the field of remote sensing, notable approaches include SatMAE [5], RVSA [46], ScaleMAE [7], and SatMAE++ [47].

CL-based foundation models. Building on the success of the pioneering work CLIP [2], multiple contrastive learning (CL) -based foundation models have been introduced in the field of remote sensing, such as RemoteCLIP [9] and GeoRSCLIP [10]. To investigate robustness with respect to different backbone sizes, we evaluate two commonly used architectures in our experiments: ViT-B/32 and ViT-L/14 [48].

LLM-based foundation models. Following the pioneering works of GPT-4 [49], MiniGPT-4 [3], and LLaVA [4], multimodal large language models (MLLMs) have attracted significant research attention in recent years. Notable approaches include GeoChat [12], LHRS-Bot [50], RS-LLaVA [51], VHM [52], SkySenseGPT [53], and Falcon [54]. In our experiments, we evaluate models with open-access code and pretrained weights for comparison.

3.1 Implementation Details

For MIM- and CLIP-based models, we take the vision backbones from pretrained foundation models and append a task-specific head (e.g., MLP, detectors, or segmentors) for each task. For these LLM-based models, since these generalist models usually freeze their vision backbones and can naturally handle multiple tasks, we directly evaluate *zero-shot* performance of these models to test their robustness.

For the scene classification task, we take the backbone from all pretrained foundation models and append a single linear layer after the backbone for classification. For the semantic segmentation (resp. detection) task, we follow RVSA [46] to use UpperNet [55] (resp. Oriented R-CNN [56]) as the segmentor (resp. detector) and replace its backbone with that from pretrained foundation models. Following RVSA [46], we take the feature maps from block 4, block 6, block 8, and block 12 to form a feature pyramid through upsampling and downsampling. We then train all comparing models for 12 epochs with an initial learning rate of 1e-5. We decay the learning rate by a factor of 0.1 at epochs 8 and 11.

For vision-language tasks, including image captioning, visual question answering, and visual grounding, we follow the original paper designs to craft task-specific prompts and evaluate the zero-shot performance of these foundation models to assess robustness. It should be noted that different pretrained foundation models are designed to accept images at specific resolutions. When the input image size differs from the pretrained backbone’s expected resolution, we interpolate the position embeddings in the backbone to accommodate the new input dimensions.

3.2 Scene Classification

From Table 1, we can draw the following findings: 1) All benchmark methods suffer from serious performance under image corruptions for the scene classification tasks, especially for MIM-based

methods. 2) CL- and LLM-based methods are more robust towards image corruptions than MIM-based methods. This is probably because CL- and LLM-based methods are trained by matching image-text pairs in a shared embedding space, learning high-level semantic features less sensitive to low-level corruptions. In contrast, MIM-based methods are trained by reconstructing pixel- or token-level details, making them sensitive to local corruptions. Specifically, VHM [52] achieves the least performance drop under image corruptions. 3) CL-based methods perform better than MIM and LLM-based methods on the scene classification task, for both clean and noisy images. Specifically, GeoRSCLIP [10] achieves the best scene classification performance under image corruptions.

Table 1: Scene classification performance on AID dataset across different image perturbations. *zs* denotes zero-shot evaluation.

Method	Backbone	Clean	Brightness Contrast	Cloud	Compression Artifacts	Data Gaps	Gauss Blur	Gauss Noise	Haze	Motion Blur	Rotate	Salt Pepper	Scale	Translate	Avg	Δ_{TP}
MIM-based																
SATLAS [57]	Swin-B	90.85	82.54	84.32	73.36	67.23	78.10	79.16	80.46	32.44	72.54	77.56	72.54	88.54	74.07	16.78
SatMAE [5]	ViT-L	72.05	44.82	59.58	67.26	46.49	71.33	71.25	28.31	63.85	69.15	70.45	59.74	66.12	59.86	12.19
Scale-MAE [7]	ViT-L	75.75	51.80	72.65	39.60	43.69	31.65	46.31	55.24	17.49	66.15	47.27	61.58	69.84	50.27	25.48
RVSA [46]	ViT-B	84.60	56.84	77.33	56.07	53.14	53.53	32.51	49.19	23.45	76.88	35.12	71.78	77.22	55.26	29.35
SatMAE++ [47]	ViT-L	91.35	64.62	82.64	62.69	60.70	48.23	76.98	62.56	29.43	85.49	73.22	75.79	87.61	67.50	23.85
CL-based																
RemoteCLIP _{zs} [9]	ViT-L	81.10	78.32	80.64	73.91	79.43	76.83	76.72	80.10	57.02	82.80	70.90	68.39	80.72	75.48	5.62
RemoteCLIP [9]	ViT-B	96.85	90.80	95.36	91.13	88.96	89.18	94.25	87.46	63.75	96.22	91.43	83.62	95.42	88.97	7.89
RemoteCLIP [9]	ViT-L	95.45	93.11	93.80	88.77	94.21	92.47	94.20	93.37	74.45	95.01	86.99	83.37	94.06	90.32	5.13
GeoRSCLIP _{zs} [10]	ViT-L	66.05	62.41	65.47	60.45	64.41	62.03	62.32	62.24	44.20	65.52	58.88	52.59	64.25	60.40	5.65
GeoRSCLIP [10]	ViT-B	96.90	93.59	96.04	91.01	93.34	92.60	92.99	92.91	57.78	95.70	88.22	75.70	93.87	88.65	8.25
GeoRSCLIP [10]	ViT-L	97.40	96.27	96.45	92.28	95.62	96.09	95.68	96.00	71.03	97.20	92.75	77.16	95.15	91.80	5.59
LLM-based																
GeoChat [12]	ViT-L	65.85	64.67	65.26	60.71	64.61	63.32	62.34	64.54	48.68	65.05	62.32	56.21	62.91	61.72	4.13
LHRS-Bot [50]	ViT-L	87.75	87.38	86.82	78.53	85.95	84.94	82.62	87.62	67.76	87.31	76.73	79.07	86.71	82.79	4.96
RS-LLaVA [51]	ViT-L	67.55	65.36	68.95	63.05	67.69	65.73	63.13	65.97	43.86	66.55	68.24	54.89	63.40	63.07	4.48
SkySenseGPT [53]	ViT-L	87.35	87.72	87.91	79.66	87.67	84.78	83.08	87.71	63.11	86.86	83.61	75.49	85.25	82.74	4.61
VHM [52]	ViT-L	80.60	79.81	80.67	76.10	80.82	78.81	76.92	79.55	59.74	80.47	75.43	72.57	79.73	76.72	3.88

3.3 Semantic Segmentation

The ISPRS Potsdam dataset provides both non-eroded and eroded labels, corresponding to annotations with and without object boundaries, respectively. In our experiments, we use the non-eroded labels for model evaluation and report the mean IoU for MIM- and CL-based methods. We omit LLM-based methods for semantic segmentation due to the lack of open-source MLLMs for this task. From Table 2, we can draw the following findings: 1) both MIM- and CL-based methods suffer from serious performance under image corruptions for the object detection task, with a mIoU drop of more than 5%. 2) MIM-based methods achieve much better performance than CL-based methods on clean and noisy images for semantic segmentation in remote sensing images. This is probably because MIM-based methods can capture local details by pixel reconstruction, while CL-based methods align global visual embeddings with text features, thus losing fine-grained details. Specifically, ScaleMAE [7] achieves the best segmentation performance under image corruption, with an average mIoU of 60.02%. 3) MIM-based methods suffer from a more serious performance drop under image corruptions than CL-based methods. Specifically, GeoRSCLIP [10] achieves the best robustness across image corruptions, with a drop of 5.15% of mIoU under corruptions.

Table 2: Semantic segmentation performance (mIoU) on the ISPRS Potsdam dataset under different image perturbations.

Method	Backbone	Clean	Brightness Contrast	Cloud	Compression Artifacts	Data Gaps	Gauss Blur	Gauss Noise	Haze	Motion Blur	Rotate	Salt Pepper	Scale	Translate	Avg	Δ_{TP}
MIM-based																
SatMAE [5]	ViT-L	59.51	50.18	37.39	48.23	51.15	57.89	41.83	44.95	57.52	56.02	36.07	54.81	59.09	49.59	9.92
ScaleMAE [7]	ViT-L	68.92	64.37	65.43	49.96	41.84	64.86	54.89	63.89	64.49	64.51	52.12	65.45	68.38	60.02	8.90
RVSA [46]	ViT-B	69.82	64.71	65.67	47.99	45.34	66.89	48.89	61.52	65.25	65.58	45.26	66.87	69.23	59.43	10.39
SatMAE++ [47]	ViT-L	62.68	53.91	59.06	49.74	53.94	60.38	44.32	48.80	60.44	58.34	39.45	58.13	61.94	54.04	8.64
CL-based																
RemoteCLIP [9]	ViT-B	50.28	42.32	45.27	39.33	37.78	50.26	48.46	36.61	50.06	46.48	46.91	48.39	49.63	45.12	5.16
RemoteCLIP [9]	ViT-L	56.69	54.51	52.73	43.24	51.19	50.82	45.12	50.47	51.82	53.68	38.98	54.59	56.53	50.31	6.38
GeoRSCLIP [10]	ViT-B	51.44	42.89	46.41	40.37	38.64	51.35	49.79	38.56	51.15	47.89	48.24	49.28	50.87	46.29	5.15
GeoRSCLIP [10]	ViT-L	56.81	54.97	52.53	43.28	41.37	50.49	42.7	49.41	51.36	53.54	36.98	54.66	56.64	48.99	7.82

3.4 Object Detection

We evaluate robustness on the corrupted images from the DIOR dataset. We report mAP for MIM- and CL-based methods. We omit LLM-based methods for the object detection task due to the lack of open-source LLMs for this task. From Table 3, we can draw the following findings: 1) both MIM-

and CL-based methods suffer from serious performance under image corruptions, with a mAP drop of more than 5%. 2) MIM- and CL-based methods achieve comparable performance for object detection on clean and noisy images. RVSA [46] attains the highest mAP of 70.96% on clean images but experiences a substantial performance decline under image corruptions. 3) MIM-based and CL-based methods exhibit a similar degree of performance degradation when subjected to image corruptions. Among them, GeoRSCLIP [10] demonstrates the most robust detection performance under noisy conditions.

Table 3: Object detection performance (mAP) on the DIOR dataset across different image perturbations.

Method	Backbone	Clean	Brightness Contrast	Cloud	Compression Artifacts	Data Gaps	Gauss Blur	Gauss Noise	Haze	Motion Blur	Rotate	Salt Pepper	Scale	Translate	Avg	Δ_{TP}
MIM-based																
SatMAE [5]	ViT-L	62.30	56.84	57.86	55.80	58.36	55.38	58.44	59.34	56.92	56.60	53.76	51.58	60.90	56.82	5.49
ScaleMAE [7]	ViT-L	70.20	64.80	65.98	62.50	64.46	62.58	63.82	66.10	63.08	63.44	60.50	53.08	68.26	63.22	6.98
RVSA [46]	ViT-B	70.96	60.59	65.02	61.58	64.60	62.35	62.87	63.98	62.88	64.04	56.61	55.97	69.69	62.51	8.45
SatMAE++ [47]	ViT-L	65.20	59.44	61.02	60.30	59.88	59.66	61.06	61.72	59.56	59.14	58.64	48.48	64.70	59.47	5.73
CL-based																
RemoteCLIP [9]	ViT-B	60.40	56.72	56.28	56.78	54.56	53.68	57.36	55.90	53.42	54.54	54.40	44.92	59.72	54.86	5.54
RemoteCLIP [9]	ViT-L	70.20	66.52	66.62	63.84	65.40	63.62	63.68	66.76	62.66	63.52	59.16	57.42	68.64	63.99	6.21
GeoRSCLIP [10]	ViT-B	60.20	56.28	56.04	56.08	55.46	53.38	56.92	55.50	53.38	53.98	53.48	46.98	59.32	54.73	5.47
GeoRSCLIP [10]	ViT-L	69.80	66.12	65.34	65.34	64.96	63.62	62.90	66.04	62.02	62.68	56.04	57.40	68.10	63.38	6.42

3.5 Image Captioning

Table 4 presents the zero-shot image captioning performance of GeoChat [12], SkySenseGPT [53], VHM [52], RS-LLaVA [51], and the recently introduced Falcon model [54]. Following the VRS-Bench protocol [26], caption quality is evaluated using the GPT-4-based CLAIR metric [58]². Given that geometric distortions—such as rotation, scaling, and translation—can substantially alter image content, we exclude performance measurements under these corruption conditions for image captioning, VQA, and visual grounding tasks.

As shown in the upper part of Table 4, all models experience performance degradation under noisy conditions. Among them, the Falcon [54] model achieves the best overall performance, significantly outperforming other methods on both clean and corrupted images, with an average performance drop of 3.89%. In contrast, RS-LLaVA [51] demonstrates the strongest robustness to image corruptions, exhibiting the smallest decrease in CLAIR score, with only a 1.04% drop. Additionally, we present results for GeoChat [12], fine-tuned on the VRSBench training set, as shown in the lower part of Table 4. The fine-tuned GeoChat model on the target dataset exhibits significantly improved performance compared to its zero-shot counterpart, but suffers from a larger performance drop under image perturbations.

Table 4: Image captioning performance (CLAIR) on the VRSBench-Cap dataset across different image perturbations. f_t denotes models trained on the VRSBench training set.

Method	Backbone	Clean	Brightness Contrast	Cloud	Compression Artifacts	Data Gaps	Gauss Blur	Gauss Noise	Haze	Motion Blur	Salt Pepper	Avg	Δ_{TP}
GeoChat [12]	ViT-L	41.39	40.06	40.45	37.65	40.20	39.76	38.48	40.38	39.92	37.61	39.59	1.80
SkySenseGPT [53]	ViT-L	48.29	47.21	46.64	44.22	46.25	45.52	44.97	46.14	45.13	44.36	45.60	2.69
VHM [52]	ViT-L	52.02	50.19	50.82	50.26	50.57	51.22	50.46	50.39	50.72	49.48	50.46	1.56
RS-LLaVA [51]	ViT-L	51.30	51.15	50.43	51.78	50.54	52.01	47.84	50.57	49.88	48.12	50.26	1.04
Falcon [54]	DaViT-B	61.90	59.98	60.09	57.13	59.48	57.43	56.31	59.85	59.94	51.83	58.01	3.89
GeoChat $_{f_t}$ [12]	ViT-L	71.26	69.00	68.93	66.60	69.45	68.63	67.83	69.98	69.02	63.87	68.15	3.11

3.6 Visual Question Answering

Table 5 reports VQA performance across various image perturbations. Following the VRSBench protocol [26], VQA performance is evaluated using the GPT-4-based matching accuracy³. From Table 5, it is evident that all LLM-based models experience a moderate decline in performance under image perturbations. Overall, VHM [52] achieves the best accuracy across both clean and noisy images. LHRs-Bot [50], RS-LLaVA [51], and Falcon [54], despite showing relatively lower overall accuracy, exhibit less sensitivity to image corruptions. Additionally, the GeoChat [12] fine-tuned on

²We use the gpt-4o-mini-2024-07-18 model to compute the CLAIR scores.

³We use the gpt-4o-mini-2024-07-18 model to compute the matching accuracy for VQA.

the VRSBench training set surpasses zero-shot models in terms of absolute performance, while also demonstrating robustness to image perturbations.

Table 5: VQA performance (Accuracy) on the VRSBench-VQA dataset across different image perturbations. *ft* indicates models fine-tuned on the VRSBench training set.

Method	Backbone	Clean	Brightness Contrast	Cloud	Compression Artifacts	Data Gaps	Gauss Blur	Gauss Noise	Haze	Motion Blur	Salt Pepper	Avg	Δ_{TP}
GeoChat [12]	ViT-L	56.63	53.89	54.82	55.14	55.99	55.88	55.44	56.22	54.08	54.04	55.06	1.57
LHRS-Bot [50]	ViT-L	35.72	35.72	35.69	35.72	35.72	35.72	35.72	35.72	35.34	35.72	35.56	0.16
SkySenseGPT [53]	ViT-L	60.21	59.26	59.73	57.93	59.64	59.21	58.27	59.63	59.17	57.27	58.90	1.31
VHM [52]	ViT-L	61.72	60.91	61.07	60.40	61.49	60.91	60.91	61.12	59.97	60.39	60.90	0.82
RS-LLaVA [51]	ViT-L	57.25	57.04	57.14	55.45	57.25	57.14	55.97	57.21	55.25	55.82	56.47	0.78
Falcon [54]	DaViT-B	33.27	32.83	32.70	32.19	33.30	33.43	32.85	32.76	32.97	31.55	32.73	0.53
GeoChat _{ft} [12]	ViT-L	75.79	75.13	74.97	73.84	75.63	74.89	74.46	75.43	74.76	72.77	74.65	1.14

3.7 Visual Grounding

Table 6 presents the zero-shot visual grounding performance of comparing methods. We report grounding accuracy at an IoU threshold of 0.5. As shown in the upper part of Table 6, all methods experience noticeable declines in performance under image perturbations. The GeoGround [59] model achieves the best performance on both clean and perturbed images, with a grounding accuracy of 75.93%. Under image perturbations, its performance declines modestly, with an average drop of 3.4%. In comparison, the Falcon [54] model, despite not being trained on VRSBench, demonstrates competitive visual grounding capability, but experiences a more significant degradation in performance when exposed to image corruptions. The fine-tuned GeoChat [12] model shows substantial improvements over its zero-shot counterpart; however, it also experiences a noticeable decline in performance under noisy conditions.

Table 6: Visual grounding performance on the VRSBench-Ref dataset across different image perturbations. We report grounding accuracy at an IoU threshold of 0.5. * indicates the GeoGround model includes VRSBench in its training data. *ft* indicates models fine-tuned on the VRSBench training set.

Method	Backbone	Clean	Brightness Contrast	Cloud	Compression Artifacts	Data Gaps	Gauss Blur	Gauss Noise	Haze	Motion Blur	Salt Pepper	Avg	Δ_{TP}
GeoChat [12]	ViT-L	18.96	17.09	16.54	16.52	16.19	16.61	16.93	17.09	16.91	16.57	16.72	2.24
VHM [52]	ViT-L	37.20	34.66	35.29	34.18	35.48	35.01	35.78	35.54	32.21	34.58	34.74	2.46
GeoGround* [59]	ViT-L	75.93	73.57	71.57	71.30	72.23	73.23	72.92	74.06	72.11	71.77	72.53	3.40
Falcon [54]	DaViT-B	73.30	71.31	69.92	65.83	68.61	70.79	64.28	71.04	68.17	59.53	67.72	5.58
GeoChat _{ft} [12]	ViT-L	55.50	53.79	52.20	50.51	53.06	53.11	51.57	54.23	52.99	49.82	52.36	3.14

4 Discussion

In this section, we further analyze the robustness of EOFMs across model architectures, tasks, corruption categories, and backbone sizes.

4.1 Vision-Centric vs. Vision-Language Foundation Models

As shown in Fig. 2, vision-centric foundation models (MIM-based) tend to suffer greater performance degradation under visual perturbations compared to vision-language models (CL- and CLM-based). This difference is especially pronounced in image-level scene classification tasks, where MIM-based models exhibit an average performance drop exceeding 20%. In contrast, vision-language models consistently demonstrate stronger robustness across tasks, maintaining performance drops below 10% in most cases. This is probably due to the complementary grounding effect of language supervision. We also note that the robustness gap between vision-centric and vision-language models is less significant for segmentation and detection tasks.

4.2 Robustness Across Different Tasks

Fig. 2 further highlights that vulnerability to perturbations varies substantially across tasks. MIM-based models are particularly sensitive in classification tasks, while CL-based models maintain

greater stability across classification, segmentation, and detection tasks. This can be attributed to the contrastive objective, which encourages learning of invariant and robust representations. LLM-based models, on the other hand, show the smallest performance degradation in vision-language tasks such as image captioning, visual question answering (VQA), and phrase grounding—typically below 3%. These results suggest that LLM-based methods excel in corruption-robust generalization, particularly in tasks that benefit from multimodal alignment.

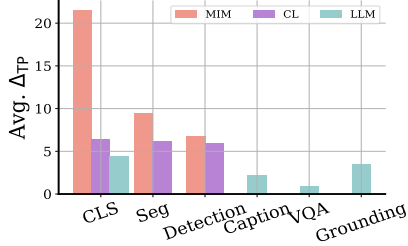


Figure 2: Robustness across different tasks and model architectures. We report the average Δ_{TP} across models.

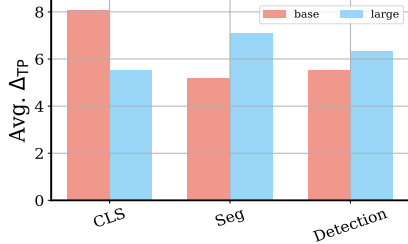


Figure 3: Robustness across different backbone sizes. We report the average Δ_{TP} for RemoteCLIP and GeoRSCLIP.

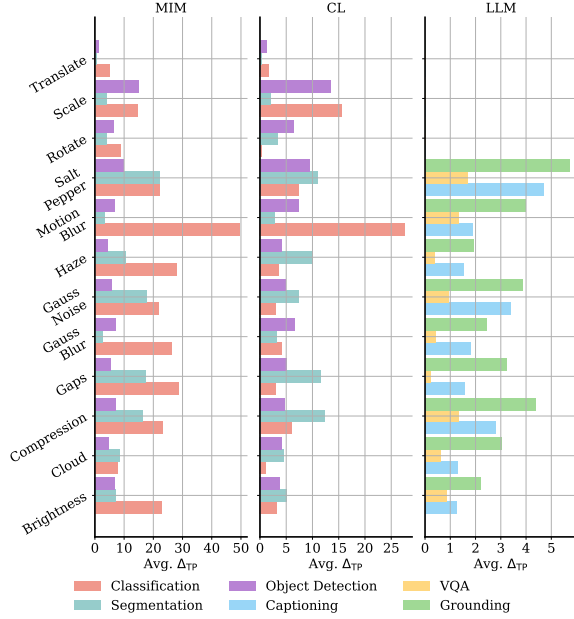


Figure 4: Robustness across different types of corruptions. We report the average Δ_{TP} across models.

4.3 Robustness Across Different Backbone Sizes

We compare the average performance of RemoteCLIP [9] and GeoRSCLIP [10] using ViT-B and ViT-L backbones across scene classification, semantic segmentation, and object detection tasks. As illustrated in Fig. 3, the impact of backbone size varies by task. For scene classification, the larger backbone (ViT-L) demonstrates greater robustness, showing less performance degradation under image corruptions. However, for fine-grained tasks such as semantic segmentation and object detection, ViT-L suffers larger performance drops compared to ViT-B. This suggests that while a larger backbone may enhance robustness in high-level recognition tasks, it may also amplify sensitivity to image corruptions in pixel- or region-level tasks.

4.4 Robustness Across Perturbation Types

As shown in Fig. 4, the performance degradation of MIM-, CL-, and LLM-based models varies notably across different visual perturbations. Motion blur causes the most severe drop, especially for MIM, which loses over 20% in performance, indicating a high sensitivity to spatial distortions. In contrast, translation has the least impact, suggesting minimal disruption to pattern recognition. Across perturbation types, LLM-based models consistently exhibit the strongest robustness, maintaining performance drops below 5% in most cases. This reinforces the value of language supervision in promoting the learning of more semantic and perturbation-invariant features.

5 Related Works

Robustness Research in Remote Sensing. Deep learning (DL)-based methods have achieved significant success in remote sensing image processing; however, their black-box nature raises concerns regarding interpretability, transparency, and vulnerability to adversarial examples. Recent studies have begun to address the robustness of DL models in this domain. Kazmi et al.[20] present a comprehensive literature review on adversarial attacks in aerial imagery processing, but do not provide an in-depth analysis of model robustness. Mei et al.[21] examine the robustness of DL-based methods for remote sensing image understanding, with a focus on image classification and object detection tasks. Lian et al. [60, 22] propose techniques to enhance adversarial robustness specifically for object detection in aerial imagery. [61] aims to improve the adversarial robustness of scene classification models in remote sensing via CAM-guided feature learning. These works only study the robustness of task-specific models. In contrast, our work for the first time investigates the robustness of foundation models in remote sensing.

Foundation Models in Remote Sensing. In general, there are four types of foundation models in remote sensing: MIM-based, CL-based, LLM-based, and diffusion-based methods. (1) Masked Image Modeling (MIM) has gained popularity through the pioneering work of MAE [1]. These methods typically employ an encoder network to learn feature representations by masking a portion of the image tokens, followed by a decoder network that reconstructs the masked image pixels in a self-supervised manner. In the field of remote sensing, notable approaches include SatMAE [5], RingMo [6], RVSA [46], ScaleMAE [7], SatMAE++ [47], and DOFA [62]. (2) Contrastive Learning (CL) employs separate encoders to project images and texts into a shared embedding space, using a contrastive objective to align the resulting embeddings. Building on the success of the pioneering work CLIP [2], several contrastive learning-based foundation models have been introduced in the field of remote sensing, including RS-CLIP [10], RemoteCLIP [9], GeoRSCLIP [10], SkyCLIP [63], S-CLIP [64], SatCLIP [65], and GeoCLIP [66]. (3) Following the pioneering works of MiniGPT-4 [3] and LLaVA [4], multimodal large language models (MLLMs) have attracted significant research attention in recent years. For instance, RSGPT [11] introduces the first GPT-based MLLM tailored for remote sensing image understanding. Other notable approaches include GeoChat [12], EarthGPT [67], EarthMarker [68], Popeye [69], RS-LLaVA [51], VHM [52], LHRS-Bot [50], SkyEyeGPT [70], SkySenseGPT [53], RSUniVLM [71], and Falcon [54]. (4) Diffusion-based foundation models learn the joint distribution between text prompts and images through a forward noising process followed by a reverse denoising process. Recent studies have applied these models to synthesize satellite [72, 73], aerial [74], hyperspectral [75], and multi-resolution imagery [76].

6 Conclusion and Future Work

In this work, we present REOBench, the first comprehensive benchmark for evaluating the robustness of EOFMs across six core tasks and twelve perturbation types. Our evaluation reveals that existing EOFMs experience noticeable performance degradation under image corruptions. We also observe significant variations in robustness across model types, task categories, and backbone sizes, offering valuable insights for future development of robust models. We hope REOBench will serve as a standard benchmark to drive the creation of more robust and reliable models for Earth observation.

Despite its contributions, this work has several limitations. First, the evaluation is limited to high-resolution optical imagery, excluding other key modalities such as multispectral (e.g., Sentinel-2), hyperspectral, and SAR data. Second, the benchmark’s dataset and task coverage are not exhaustive. While it includes widely used datasets (AID, Potsdam, DIOR, VRSBench), they may not fully reflect global variation in geography, resolution, or sensor types. Additionally, important tasks such as change detection, region captioning, and object counting are currently not included.

7 Broader Impact

REOBench aims to improve the reliability of Earth observation foundation models by systematically evaluating their robustness to real-world noise and perturbations. This is critical for high-stakes applications such as disaster response and environmental monitoring. By identifying vulnerability patterns across tasks and models, our benchmark can guide the development of future robust models.

References

- [1] Kaiming He, Xinlei Chen, Saining Xie, Yanghao Li, Piotr Dollár, and Ross Girshick. Masked autoencoders are scalable vision learners. In *Proceedings of the IEEE/CVF conference on computer vision and pattern recognition*, pages 16000–16009, 2022.
- [2] Alec Radford, Jong Wook Kim, Chris Hallacy, Aditya Ramesh, Gabriel Goh, Sandhini Agarwal, Girish Sastry, Amanda Askell, Pamela Mishkin, Jack Clark, et al. Learning transferable visual models from natural language supervision. In *International conference on machine learning*, pages 8748–8763. PmLR, 2021.
- [3] Deyao Zhu, Jun Chen, Xiaoqian Shen, Xiang Li, and Mohamed Elhoseiny. MiniGPT-4: Enhancing vision-language understanding with advanced large language models. In *The Twelfth International Conference on Learning Representations*, 2024.
- [4] Haotian Liu, Chunyuan Li, Qingyang Wu, and Yong Jae Lee. Visual instruction tuning. *Advances in neural information processing systems*, 36:34892–34916, 2023.
- [5] Yezhen Cong, Samar Khanna, Chenlin Meng, Patrick Liu, Erik Rozi, Yutong He, Marshall Burke, David Lobell, and Stefano Ermon. SatMAE: Pre-training transformers for temporal and multi-spectral satellite imagery. *Advances in Neural Information Processing Systems*, 35:197–211, 2022.
- [6] Xian Sun, Peijin Wang, Wanxuan Lu, Zicong Zhu, Xiaonan Lu, Qibin He, Junxi Li, Xuee Rong, Zhujun Yang, Hao Chang, et al. RingMo: A remote sensing foundation model with masked image modeling. *IEEE Transactions on Geoscience and Remote Sensing*, 61:1–22, 2022.
- [7] Colorado J Reed, Ritwik Gupta, Shufan Li, Sarah Brockman, Christopher Funk, Brian Clipp, Kurt Keutzer, Salvatore Candido, Matt Uyttendaele, and Trevor Darrell. Scale-MAE: A scale-aware masked autoencoder for multiscale geospatial representation learning. In *Proceedings of the IEEE/CVF International Conference on Computer Vision*, pages 4088–4099, 2023.
- [8] Danfeng Hong, Bing Zhang, Xuyang Li, Yuxuan Li, Chenyu Li, Jing Yao, Naoto Yokoya, Hao Li, Pedram Ghamisi, Xiuping Jia, et al. SpectralGPT: Spectral remote sensing foundation model. *IEEE Transactions on Pattern Analysis and Machine Intelligence*, 2024.
- [9] Fan Liu, Delong Chen, Zhangqingyun Guan, Xiaocong Zhou, Jiale Zhu, Qiaolin Ye, Liyong Fu, and Jun Zhou. RemoteCLIP: A vision language foundation model for remote sensing. *IEEE Transactions on Geoscience and Remote Sensing*, 2024.
- [10] Zilun Zhang, Tiancheng Zhao, Yulong Guo, and Jianwei Yin. RS5M and GeoRSCLIP: A large scale vision-language dataset and a large vision-language model for remote sensing. *IEEE Transactions on Geoscience and Remote Sensing*, 2024.
- [11] Yuan Hu, Jianlong Yuan, Congcong Wen, Xiaonan Lu, Yu Liu, and Xiang Li. RSGPT: A remote sensing vision language model and benchmark. *ISPRS Journal of Photogrammetry and Remote Sensing*, 224:272–286, 2025.
- [12] Kartik Kuckreja, Muhammad Sohail Danish, Muzammal Naseer, Abhijit Das, Salman Khan, and Fahad Shahbaz Khan. GeoChat: Grounded large vision-language model for remote sensing. In *Proceedings of the IEEE/CVF Conference on Computer Vision and Pattern Recognition*, pages 27831–27840, 2024.
- [13] Licheng Jiao, Zhongjian Huang, Xiaoqiang Lu, Xu Liu, Yuting Yang, Jiaxuan Zhao, Jinyue Zhang, Biao Hou, Shuyuan Yang, Fang Liu, et al. Brain-inspired remote sensing foundation models and open problems: A comprehensive survey. *IEEE Journal of Selected Topics in Applied Earth Observations and Remote Sensing*, 16:10084–10120, 2023.
- [14] Xiang Li, Congcong Wen, Yuan Hu, Zhenghang Yuan, and Xiao Xiang Zhu. Vision-language models in remote sensing: Current progress and future trends. *IEEE Geoscience and Remote Sensing Magazine*, 2024.
- [15] Xiao Xiang Zhu, Zhitong Xiong, Yi Wang, Adam J Stewart, Konrad Heidler, Yuanyuan Wang, Zhenghang Yuan, Thomas Dujardin, Qingsong Xu, and Yilei Shi. On the foundations of earth and climate foundation models. *arXiv preprint arXiv:2405.04285*, 2024.
- [16] Aoran Xiao, Weihao Xuan, Junjue Wang, Jiaying Huang, Dacheng Tao, Shijian Lu, and Naoto Yokoya. Foundation models for remote sensing and earth observation: A survey. *arXiv preprint arXiv:2410.16602*, 2024.

- [17] Siqu Lu, Junlin Guo, James R Zimmer-Dauphinee, Jordan M Nieusma, Xiao Wang, Steven A Wernke, Yuankai Huo, et al. Vision foundation models in remote sensing: A survey. *IEEE Geoscience and Remote Sensing Magazine*, 2025.
- [18] Chunlei Huo, Keming Chen, Shuaihao Zhang, Zeyu Wang, Heyu Yan, Jing Shen, Yuyang Hong, Geqi Qi, Hongmei Fang, and Zihan Wang. When remote sensing meets foundation model: A survey and beyond. *remote sensing*, 17(2), 2025.
- [19] Ziyue Huang, Hongxi Yan, Qiqi Zhan, Shuai Yang, Mingming Zhang, Chenkai Zhang, YiMing Lei, Zeming Liu, Qingjie Liu, and Yunhong Wang. A survey on remote sensing foundation models: From vision to multimodality. *arXiv preprint arXiv:2503.22081*, 2025.
- [20] Syed M. Kazam Abbas Kazmi, Nayyer Aafaq, Mansoor Ahmad Khan, Ammar Saleem, and Zahid Ali. Adversarial attacks on aerial imagery: The state-of-the-art and perspective. *2023 3rd International Conference on Artificial Intelligence (ICAI)*, pages 95–102, 2023.
- [21] Shaohui Mei, Jiawei Lian, Xiaofei Wang, Yuru Su, Mingyang Ma, and Lap-Pui Chau. A comprehensive study on the robustness of image classification and object detection in remote sensing: Surveying and benchmarking. *ArXiv*, abs/2306.12111, 2023.
- [22] Jiawei Lian, Shaohui Mei, Shun Zhang, and Mingyang Ma. Benchmarking adversarial patch against aerial detection. *IEEE Transactions on Geoscience and Remote Sensing*, 60:1–16, 2022.
- [23] Gui-Song Xia, Jingwen Hu, Fan Hu, Baoguang Shi, Xiang Bai, Yanfei Zhong, Liangpei Zhang, and Xiaoqiang Lu. AID: A benchmark data set for performance evaluation of aerial scene classification. *IEEE Transactions on Geoscience and Remote Sensing*, 55(7):3965–3981, 2017.
- [24] Franz Rottensteiner, Gunho Sohn, Jaewook Jung, Markus Gerke, Caroline Baillard, Sebastien Benitez, and Uwe Breitkopf. The ISPRS benchmark on urban object classification and 3D building reconstruction. *ISPRS Annals of the Photogrammetry, Remote Sensing and Spatial Information Sciences; I-3*, 1(1):293–298, 2012.
- [25] Ke Li, Gang Wan, Gong Cheng, Liqiu Meng, and Junwei Han. Object detection in optical remote sensing images: A survey and a new benchmark. *ISPRS journal of photogrammetry and remote sensing*, 159:296–307, 2020.
- [26] Xiang Li, Jian Ding, and Mohamed Elhoseiny. VRSBench: A versatile vision-language benchmark dataset for remote sensing image understanding. In *The Thirty-eight Conference on Neural Information Processing Systems Datasets and Benchmarks Track*, 2024.
- [27] Jacob Høxbroe Jeppesen, Rune Hylsberg Jacobsen, Fadil Inceoglu, and Thomas Skjødeberg Toftegaard. A cloud detection algorithm for satellite imagery based on deep learning. *Remote sensing of environment*, 229:247–259, 2019.
- [28] Vishnu Sarukkai, Anirudh Jain, Burak Uzkent, and Stefano Ermon. Cloud removal from satellite images using spatiotemporal generator networks. In *Proceedings of the IEEE/CVF Winter Conference on Applications of Computer Vision*, pages 1796–1805, 2020.
- [29] Liangpei Zhang, Gui-Song Xia, Tianfu Wu, Liang Lin, Xue-Cheng Tai, et al. Deep learning for remote sensing image understanding. *J. Sensors*, 2016(2):1–2, 2016.
- [30] Thomas Müller and Bastian Erdnūß. Brightness correction and shadow removal for video change detection with uavs. In *Autonomous systems: sensors, processing, and security for vehicles and infrastructure 2019*, volume 11009, page 1100906. SPIE, 2019.
- [31] Aliaksei Makarau, Rudolf Richter, Rupert Müller, and Peter Reinartz. Haze detection and removal in remotely sensed multispectral imagery. *IEEE Transactions on Geoscience and Remote Sensing*, 52(9):5895–5905, 2014.
- [32] Yuanyuan Li, Qiyang Ling, Yiyao An, Hongpeng Yin, Xinbo Gao, Zhiqin Zhu, and Peng Han. DHC-Net: A remote sensing object detection under haze and class imbalance. *IEEE Transactions on Geoscience and Remote Sensing*, 2025.
- [33] Dan Hendrycks and Thomas Dietterich. Benchmarking neural network robustness to common corruptions and perturbations. In *International Conference on Learning Representations*, 2019.
- [34] Till Sieberth, Rene Wackrow, and JH Chandler. UAV image blur—its influence and ways to correct it. *The International Archives of the Photogrammetry, Remote Sensing and Spatial Information Sciences*, 40:33–39, 2015.

- [35] Till Sieberth, Rene Wackrow, and JH Chandler. Influence of blur on feature matching and a geometric approach for photogrammetric deblurring. *The International Archives of the Photogrammetry, Remote Sensing and Spatial Information Sciences*, 40:321–326, 2014.
- [36] T Sieberth, R Wackrow, and JH Chandler. Motion blur disturbs—the influence of motion-blurred images in photogrammetry. *The Photogrammetric Record*, 29(148):434–453, 2014.
- [37] Sornkitja Boonprong, Chunxiang Cao, Wei Chen, Xiliang Ni, Min Xu, and Bipin Kumar Acharya. The classification of noise-afflicted remotely sensed data using three machine-learning techniques: effect of different levels and types of noise on accuracy. *ISPRS International Journal of Geo-Information*, 7(7):274, 2018.
- [38] Ram M Narayanan, Sudhir K Ponnappan, and Stephen E Reichenbach. Effects of noise on the information content of remote sensing images. *Geocarto International*, 18(2):15–26, 2003.
- [39] Jin Chen, Xiaolin Zhu, James E Vogelmann, Feng Gao, and Suming Jin. A simple and effective method for filling gaps in landsat ETM+ SLC-off images. *Remote sensing of environment*, 115(4):1053–1064, 2011.
- [40] Feng Chen, Xiaofeng Zhao, Hong Ye, and Zdravko Karakehayov. Making use of the landsat 7 SLC-off etm+ image through different recovering approaches. *Data Acquisition Applications*, pages 317–342, 2012.
- [41] Tajeddine Benbarrad, Lamiae Eloutouate, Mounir Arioua, Fatiha Elouaai, and My Driss Laanaoui. Impact of image compression on the performance of steel surface defect classification with a CNN. *Journal of Sensor and Actuator Networks*, 10(4):73, 2021.
- [42] Yinpeng Dong, Caixin Kang, Jinlai Zhang, Zijian Zhu, Yikai Wang, Xiao Yang, Hang Su, Xingxing Wei, and Jun Zhu. Benchmarking robustness of 3D object detection to common corruptions. In *Proceedings of the IEEE/CVF Conference on Computer Vision and Pattern Recognition*, pages 1022–1032, 2023.
- [43] Jian Kang, Ruben Fernandez-Beltran, Zhirui Wang, Xian Sun, Jingen Ni, and Antonio Plaza. Rotation-invariant deep embedding for remote sensing images. *IEEE Transactions on Geoscience and Remote Sensing*, 60:1–13, 2021.
- [44] Wei Han, Jun Li, Sheng Wang, Yi Wang, Jining Yan, Runyu Fan, Xiaohan Zhang, and Lizhe Wang. A context-scale-aware detector and a new benchmark for remote sensing small weak object detection in unmanned aerial vehicle images. *International Journal of Applied Earth Observation and Geoinformation*, 112:102966, 2022.
- [45] Wooju Lee, Donggyu Sim, and Seoung-Jun Oh. A CNN-based high-accuracy registration for remote sensing images. *Remote Sensing*, 13(8):1482, 2021.
- [46] Di Wang, Qiming Zhang, Yufei Xu, Jing Zhang, Bo Du, Dacheng Tao, and Liangpei Zhang. Advancing plain vision transformer toward remote sensing foundation model. *IEEE Transactions on Geoscience and Remote Sensing*, 61:1–15, 2022.
- [47] Mubashir Noman, Muzammal Naseer, Hisham Cholakkal, Rao Muhammad Anwer, Salman Khan, and Fahad Shahbaz Khan. Rethinking transformers pre-training for multi-spectral satellite imagery. In *Proceedings of the IEEE/CVF Conference on Computer Vision and Pattern Recognition*, pages 27811–27819, 2024.
- [48] Alexey Dosovitskiy, Lucas Beyer, Alexander Kolesnikov, Dirk Weissenborn, Xiaohua Zhai, Thomas Unterthiner, Mostafa Dehghani, Matthias Minderer, Georg Heigold, Sylvain Gelly, et al. An image is worth 16x16 words: Transformers for image recognition at scale. In *International Conference on Learning Representations*, 2021.
- [49] OpenAI. GPT-4 technical report, 2023.
- [50] Dilxat Muhtar, Zhenshi Li, Feng Gu, Xuiliang Zhang, and Pengfeng Xiao. LHRS-Bot: Empowering remote sensing with VGI-enhanced large multimodal language model. In *European Conference on Computer Vision*, pages 440–457. Springer, 2024.
- [51] Yakoub Bazi, Laila Bashmal, Mohamad Mahmoud Al Rahhal, Riccardo Ricci, and Farid Melgani. RS-LLaVA: A large vision-language model for joint captioning and question answering in remote sensing imagery. *Remote Sensing*, 16(9):1477, 2024.
- [52] Chao Pang, Xingxing Weng, Jiang Wu, Jiayu Li, Yi Liu, Jiaying Sun, Weijia Li, Shuai Wang, Litong Feng, Gui-Song Xia, et al. VHM: Versatile and honest vision language model for remote sensing image analysis. In *Proceedings of the AAAI Conference on Artificial Intelligence*, volume 39, pages 6381–6388, 2025.

- [53] Junwei Luo, Zhen Pang, Yongjun Zhang, Tingzhu Wang, Linlin Wang, Bo Dang, Jiangwei Lao, Jian Wang, Jingdong Chen, Yihua Tan, et al. SkySenseGPT: A fine-grained instruction tuning dataset and model for remote sensing vision-language understanding. *arXiv preprint arXiv:2406.10100*, 2024.
- [54] Kelu Yao, Nuo Xu, Rong Yang, Yingying Xu, Zhuoyan Gao, Titinunt Kitrungrotsakul, Yi Ren, Pu Zhang, Jin Wang, Ning Wei, et al. Falcon: A remote sensing vision-language foundation model. *arXiv preprint arXiv:2503.11070*, 2025.
- [55] Tete Xiao, Yingcheng Liu, Bolei Zhou, Yuning Jiang, and Jian Sun. Unified perceptual parsing for scene understanding. In *Proceedings of the European conference on computer vision (ECCV)*, pages 418–434, 2018.
- [56] Xingxing Xie, Gong Cheng, Jiabao Wang, Xiwen Yao, and Junwei Han. Oriented R-CNN for object detection. In *Proceedings of the IEEE/CVF international conference on computer vision*, pages 3520–3529, 2021.
- [57] Favien Bastani, Piper Wolters, Ritwik Gupta, Joe Ferdinando, and Aniruddha Kembhavi. SatlasPretrain: A large-scale dataset for remote sensing image understanding. In *Proceedings of the IEEE/CVF International Conference on Computer Vision*, pages 16772–16782, 2023.
- [58] David Chan, Suzanne Petryk, Joseph Gonzalez, Trevor Darrell, and John Canny. CLAIR: Evaluating image captions with large language models. In *Proceedings of the 2023 Conference on Empirical Methods in Natural Language Processing*, pages 13638–13646, 2023.
- [59] Yue Zhou, Mengcheng Lan, Xiang Li, Yiping Ke, Xue Jiang, Litong Feng, and Wayne Zhang. GeoGround: A unified large vision-language model for remote sensing visual grounding. *arXiv preprint arXiv:2411.11904*, 2024.
- [60] Jiawei Lian, Xiaofei Wang, Yuru Su, Mingyang Ma, and Shaohui Mei. CBA: Contextual background attack against optical aerial detection in the physical world. *IEEE Transactions on Geoscience and Remote Sensing*, 61:1–16, 2023.
- [61] Sumaiya Tasneem and Kazi Aminul Islam. Improve adversarial robustness of ai models in remote sensing via data-augmentation and explainable-ai methods. *Remote. Sens.*, 16:3210, 2024.
- [62] Zhitong Xiong, Yi Wang, Fahong Zhang, Adam J Stewart, Joëlle Hanna, Damian Borth, Ioannis Papoutsis, Bertrand Le Saux, Gustau Camps-Valls, and Xiao Xiang Zhu. Neural plasticity-inspired multimodal foundation model for earth observation. *arXiv preprint arXiv:2403.15356*, 2024.
- [63] Zhecheng Wang, Rajanie Prabha, Tianyuan Huang, Jiajun Wu, and Ram Rajagopal. SkyScript: A large and semantically diverse vision-language dataset for remote sensing. In *Proceedings of the AAAI Conference on Artificial Intelligence*, volume 38, pages 5805–5813, 2024.
- [64] Sangwoo Mo, Minkyu Kim, Kyungmin Lee, and Jinwoo Shin. S-CLIP: Semi-supervised vision-language learning using few specialist captions. In *Neural Information Processing Systems*, 2023.
- [65] Konstantin Klemmer, Esther Rolf, Caleb Robinson, Lester Mackey, and Marc Rußwurm. SatCLIP: Global, general-purpose location embeddings with satellite imagery. In *Proceedings of the AAAI Conference on Artificial Intelligence*, volume 39, pages 4347–4355, 2025.
- [66] Vicente Vivanco Cepeda, Gaurav Kumar Nayak, and Mubarak Shah. GeoCLIP: Clip-inspired alignment between locations and images for effective worldwide geo-localization. *Advances in Neural Information Processing Systems*, 36:8690–8701, 2023.
- [67] Wei Zhang, Miaoxin Cai, Tong Zhang, Yin Zhuang, and Xuerui Mao. EarthGPT: A universal multi-modal large language model for multi-sensor image comprehension in remote sensing domain. *IEEE Transactions on Geoscience and Remote Sensing*, 2024.
- [68] Wei Zhang, Miaoxin Cai, Tong Zhang, Yin Zhuang, Jun Li, and Xuerui Mao. EarthMarker: A visual prompting multi-modal large language model for remote sensing. *IEEE Transactions on Geoscience and Remote Sensing*, 2024.
- [69] Wei Zhang, Miaoxin Cai, Tong Zhang, Guoqiang Lei, Yin Zhuang, and Xuerui Mao. Popeye: A unified visual-language model for multi-source ship detection from remote sensing imagery. *IEEE Journal of Selected Topics in Applied Earth Observations and Remote Sensing*, 2024.
- [70] Yang Zhan, Zhitong Xiong, and Yuan Yuan. SkyEyeGPT: Unifying remote sensing vision-language tasks via instruction tuning with large language model. *ISPRS Journal of Photogrammetry and Remote Sensing*, 221:64–77, 2025.

- [71] Xu Liu and Zhouhui Lian. RSUniVLM: A unified vision language model for remote sensing via granularity-oriented mixture of experts. *arXiv preprint arXiv:2412.05679*, 2024.
- [72] Samar Khanna, Patrick Liu, Linqi Zhou, Chenlin Meng, Robin Rombach, Marshall Burke, David B. Lobell, and Stefano Ermon. DiffusionSat: A generative foundation model for satellite imagery. In *The Twelfth International Conference on Learning Representations*, 2024.
- [73] Chenyang Liu, Ke-Yu Chen, Ruiyun Zhao, Zhengxia Zou, and Zhen Xia Shi. Text2Earth: Unlocking text-driven remote sensing image generation with a global-scale dataset and a foundation model. *ArXiv*, abs/2501.00895, 2025.
- [74] Ahmad Arrabi, Xiaohan Zhang, Waqas Sultani, Chen Chen, and Safwan Wshah. Cross-view meets diffusion: Aerial image synthesis with geometry and text guidance. *2025 IEEE/CVF Winter Conference on Applications of Computer Vision (WACV)*, pages 5356–5366, 2024.
- [75] Li Pang, Datao Tang, Shuang Xu, Deyu Meng, and Xiangyong Cao. HSiGene: A foundation model for hyperspectral image generation. *ArXiv*, abs/2409.12470, 2024.
- [76] Zhiping Yu, Chenyang Liu, Liqin Liu, Zhen Xia Shi, and Zhengxia Zou. MetaEarth: A generative foundation model for global-scale remote sensing image generation. *IEEE Transactions on Pattern Analysis and Machine Intelligence*, 47:1764–1781, 2024.
- [77] Raouf Touti. Perlin noise: A procedural generation algorithm, 2017.
- [78] Diederik P Kingma. Adam: A method for stochastic optimization. *arXiv preprint arXiv:1412.6980*, 2014.
- [79] Ilya Loshchilov and Frank Hutter. Sgdr: Stochastic gradient descent with warm restarts. *arXiv preprint arXiv:1608.03983*, 2016.
- [80] MMSegmentation Contributors. Mmsegmentation: Openmmlab semantic segmentation toolbox and benchmark, 2020.
- [81] Ilya Loshchilov and Frank Hutter. Decoupled weight decay regularization. *arXiv preprint arXiv:1711.05101*, 2017.
- [82] Yue Zhou, Xue Yang, Gefan Zhang, Jiabao Wang, Yanyi Liu, Liping Hou, Xue Jiang, Xingzhao Liu, Junchi Yan, Chengqi Lyu, et al. Mmrotate: A rotated object detection benchmark using pytorch. In *Proceedings of the 30th ACM International Conference on Multimedia*, pages 7331–7334, 2022.

A REOBench Documentation and Intended Uses

A.1 Overview

REOBench dataset includes four subsets: AID for scene classification, ISPRS Potsdam for semantic segmentation, DIOR for object detection, and VRSBench for image captioning, visual question answering (VQA), and visual grounding.

A.2 Data Organization

Our REOBench dataset is organized as follows.

```
root/
├── AID
│   ├── AID_train.zip
│   ├── AID_test.zip
│   └── AID_JSON
├── Potsdam
│   ├── Potsdam_Images_train.zip
│   ├── Potsdam_Anns_train.zip
│   ├── Potsdam_Images_test.zip
│   └── Potsdam_Anns_test.zip
├── DIOR
│   ├── DIOR_Images_train.zip
│   ├── DIOR_Anns_train.zip
│   ├── DIOR_Images_test
│   │   ├── clean.zip; brightness_contrast.zip; cloud.zip;
│   │   │   compression_artifacts.zip...
│   ├── DIOR_Anns_test
│   │   ├── clean.zip; rotate.zip; scale.zip; translate.zip
├── VRSBench
│   ├── VRSBench_Images_train.zip
│   ├── VRSBench_train.json
│   ├── VRSBench_Images_test
│   │   ├── clean.zip; brightness_contrast.zip; cloud.zip;
│   │   │   compression_artifacts.zip...
│   ├── VRSBench_EVAL_Cap.json
│   ├── VRSBench_EVAL_referring.json
│   └── VRSBench_EVAL_vqa.json
```

Detailed descriptions for each folder or file are given below.

- AID/Images_train.zip contains all AID images in the training set.
- AID/Images_test.zip contains images in the test set under corruption.
- AID/AID_JSON folder contains json file for zero-shot evaluation of LLM-based models.
- Potsdam/Potsdam_Images_train.zip contains all Potsdam images in the training set.
- Potsdam/Potsdam_Images_train.zip contains all Potsdam images in the test set under corruption.
- Potsdam/Potsdam_Anns_train.zip contains annotations for images in the training set.
- Potsdam/Potsdam_Anns_test.zip contains annotations for images in the test set under corruption.
- DIOR/DIOR_Images_train.zip contains all DIOR images in the training set.
- DIOR/DIOR_Anns_train.zip contains all Oriented Bounding Boxes annotations for images in the training set.
- DIOR/DIOR_Images_test folder contains all DIOR images in the test set under corruption.
- DIOR/DIOR_Anns_test folder contains oriented bounding box annotations for test images under four settings: clean, and three spatial transformations — rotate, scale, and translate.

For corruptions that do not involve spatial transformations (e.g., blur, noise), annotations from the clean setting are reused, as these corruptions do not alter object positions or shapes.

- VRSBench/Annotation_Images_train.zip contains VRSBench images in the training set.
- VRSBench/Annotation_Images_test folder contains VRSBench images in the test set, one folder per noise type.
- VRSBench/VRSBench_train.json contains VRSBench training annotations following LLaVA in standard JSON format.
- VRSBench/VRSBench_EVAL_Cap.json contains VRSBench evaluation annotations for the captioning task in standard JSON format.
- VRSBench/VRSBench_EVAL_referring.json contains VRSBench evaluation annotations for the visual grounding task in standard JSON format.
- VRSBench/VRSBench_EVAL_vqa.json contains VRSBench evaluation annotations for the VQA task in standard JSON format.

A.3 Intended Uses

REOBench is intended for use in academic and research settings, specifically for:

- Evaluating the robustness of remote sensing foundation models.
- Understand the robustness of remote sensing foundation models across tasks, noise types, and model architectures.

A.4 Use Cases

- **Robustness Research:** REOBench provides a standardized testbed for evaluating the robustness of remote sensing foundation models under a wide range of realistic corruptions, making it valuable for both academic and applied robustness research.
- **Model Diagnosis and Comparison:** The benchmark enables fine-grained analysis of performance degradation across different model types (e.g., MIM-based, CL-based, LLM-based), tasks, and corruption types, serving as a practical tool for diagnosing model vulnerabilities and comparing architectures.
- **Guidance for Model Development:** Insights derived from REOBench can inform the design of more resilient remote sensing models and training strategies, particularly for mission-critical applications such as disaster response and environmental monitoring.

A.5 Limitations

- **Modal and Sensor Scope:** This benchmark focuses exclusively on optical remote sensing imagery and does not currently include multispectral, hyperspectral, or SAR modalities, limiting its applicability to other sensing systems.
- **Task Coverage:** While REOBench includes six core tasks, it does not encompass important tasks such as change detection, region captioning, and object counting, which are increasingly relevant in Earth observation.
- **Dataset Representativeness:** The benchmark is constructed from well-known datasets such as AID, DIOR, Potsdam, and VRSBench, which may not fully capture the geographic, temporal, and sensor diversity of real-world global remote sensing data.

A.6 Ethical Considerations

- **Public Data Usage:** REOBench is built entirely from publicly available datasets. No personal, private, or sensitive information is included, and care has been taken to respect privacy in all sourced imagery.
- **Responsible Use:** We encourage the research community to use this benchmark ethically, particularly in downstream applications involving environmental monitoring, urban analytics, and decision-making systems that may influence public policy or resource allocation.

A.7 Documentation and Maintenance

- **Versioning:** Detailed version history of the dataset will be maintained to track changes and improvements over time.
- **Version Control:** The benchmark will be versioned to ensure transparency in updates, including bug fixes, additional corruption types, and task expansions.
- **Community Feedback:** We welcome contributions and suggestions from the community to expand, refine, and validate the benchmark, fostering collaborative progress in building robust AI systems for Earth observation.

A.8 Accountability Framework

To promote responsible AI development, REOBench adopts an open accountability model. Users are encouraged to report any issues related to dataset quality, annotation errors, or robustness evaluation inconsistencies. These reports will be reviewed and integrated into future updates, supporting a continuous feedback loop for improving the benchmark’s accuracy, fairness, and utility.

B URL to Data and Metadata

The REOBench dataset can be accessed and downloaded through our Huggingface repository (<https://huggingface.co/datasets/xiang709/REOBench>). Detailed metadata for the dataset is documented using the Croissant metadata framework, ensuring comprehensive coverage and compliance with the MLCommons Croissant standards, check [metadata](<https://huggingface.co/api/datasets/xiang709/REOBench>).

C Author Statement and Data License

Author Responsibility Statement: The authors bear all responsibilities in case of any violations of rights or ethical concerns regarding the REOBench dataset.

Data License Confirmation: The dataset is released under the [CC-BY-4.0], which permits unrestricted use, distribution, and reproduction in any medium, provided the original work is properly cited.

D Hosting and Accessibility

The REOBench dataset is hosted on Huggingface (<https://huggingface.co/datasets/xiang709/REOBench>) to ensure reliable and continuous accessibility.

Maintenance Plan: Ongoing maintenance and updates will be managed by the dataset authors, with updates scheduled bi-annually or as significant changes in the data sources occur.

Long-term Preservation: The dataset is archived in Huggingface (<https://huggingface.co/datasets/xiang709/REOBench>) to ensure long-term availability.

Structured Metadata: The annotation for each image is well-organized in standard JSON format to ensure easy usage.

E Dataset Collection Details

E.1 Source datasets

Our REOBench uses three source datasets, i.e., AID for scene classification, ISPRS Potsdam for semantic segmentation, DIOR for object detection, and VRSBench for image captioning, visual question answering (VQA), and visual grounding. The details of each dataset are shown in Table 7.

Table 7: Statistics of source datasets.

Dataset	Train	Test	Category	Size
AID	8,000	2,000	30	256×256
Potsdam	3,456	2,016	6	512×512
DIOR-R	11,725	11,738	20	800×800
VRSBench	20,264	9,350	26	512×512

Table 8: Configurations of different image corruption types and corresponding severity.

Corruption Type	Parameter	S1	S2	S3	S4	S5
Gaussian Noise	σ	0.04	0.05	0.06	0.07	0.08
Salt Pepper Noise	amount	0.005	0.01	0.02	0.03	0.05
Gaussian Blur	kernel size	3 \times 3	5 \times 5	7 \times 7	9 \times 9	11 \times 11
Motion Blur	kernel size	2 \times 2	4 \times 4	6 \times 6	8 \times 8	10 \times 10
Brightness/Contrast	b / c	+0.0 / 1.0	+0.1 / 0.8	+0.2 / 0.6	+0.3 / 0.4	+0.4 / 0.2
Clouds	threshold	0.90	0.85	0.80	0.75	0.70
Haze	intensity	0.20	0.30	0.40	0.50	0.60
Data Gaps	num / width (px)	2 / 3	3 / 4	4 / 5	5 / 6	6 / 7
Compression Artifacts	JPEG quality	30	25	20	15	10
Rotation	angle ($^{\circ}$)	30	45	60	75	90
Scaling	scale ratio	0.9	0.8	0.7	0.6	0.5
Translation	displacement (px)	± 15	± 20	± 25	± 30	± 35

E.2 Image Perturbations

In table 8, we report parameter configures for different noise levels and types. S1 to S5 represent the severity levels of each corruption, with S1 being the mildest and S5 the most severe. The ‘‘Parameter’’ column lists the key control variables for each type of image corruption. For Gaussian noise, σ represents the standard deviation that controls the amplitude of the Gaussian noise; for salt-and-pepper noise, the amount specifies the proportion of pixels randomly replaced with black or white; Gaussian blur and motion blur use kernel size to define the size of the convolution kernel; brightness and contrast corruption is controlled using b/c to represent brightness offset and contrast scaling respectively; for the cloud corruption, density denotes the cloud coverage, which is controlled based on the Perlin noise threshold [77]; the parameter for haze simulation is intensity, a blending ratio that determines the degree of mixing with a white layer; data gaps are defined by number/width of stripes, which specifies the number and width of missing regions; Compression Artifacts are governed by the JPEG quality parameter, with lower values indicating stronger compression artifacts. In terms of geometric transformations, rotation is defined by angle, scaling is represented by scale ratio, and translation is described by the maximum offset in displacement. These parameters allow for systematic control and severity grading of each corruption type.

F More Experimental Results

F.1 More Implementation Details

Table 9 lists training configurations for different tasks. For the scene classification task, all experiments are conducted on a single NVIDIA RTX 4090 GPU with 24 GB of memory, using the AID dataset, which contains 10,000 high-resolution aerial images. The dataset is split into 8,000 training samples and 2,000 testing samples, with all images uniformly resized to 256×256 pixels. All models are trained for 100 epochs using the Adam [78] optimizer with an initial learning rate of $1e-3$ and a batch size of 16. A CosineAnnealingWarmRestarts [79] scheduler is employed, with the initial cycle length set to 5 epochs.

For the semantic segmentation task, all experiments are conducted on a single NVIDIA A100 GPU with 40 GB of memory. The experiments are implemented using the MMSegmentation [80] framework, with UPerHead used as the primary decoder head and FCNHead as the auxiliary head. All training and evaluation are performed on the Potsdam dataset, where each original image ($6,000 \times 6,000$ pixels) is divided into 144 non-overlapping patches of 512×512 pixels for model training and inference. The resulting dataset comprises 5,472 image patches, split into 3,456 samples for training

and 2,016 for testing. Training is performed for 12 epochs using the AdamW optimizer [81], with an initial learning rate of $6e-5$, a batch size of 8, and a weight decay of 0.05.

For the object detection task, all experiments are conducted on a single NVIDIA A100 GPU with 80 GB of memory. The experiments are implemented using the MMRotate framework [82], with Oriented R-CNN employed as the detection head. All images in the DIOR-R dataset are resized to 800×800 pixels. The official trainval split is used for training, while the test split is used for both clean evaluation and as the basis for our noise-augmented test set. For fine-tuning, we extracted the last-layer feature map from each model’s pretrained backbone and constructed a four-level feature pyramid via up/down-sampling, which is then fed into a newly initialized Oriented R-CNN head. The detector is trained for 12 epochs using the AdamW optimizer [81], with an initial learning rate of $1e-5$, a batch size of 1, and a learning rate decay of 0.1 applied at epochs 8 and 11.

Table 9: Training configurations for different tasks.

	Scene Classification	Semantic Segmentation	Object Detection
Dataset	AID	Potsdam	DIOR-R
Decoder	Linear	UpperNet	Oriented R-CNN
Optimizer	Adam	AdamW	AdamW
Epochs	100	12	12
Lr	$1e-3$	$6e-5$	$1e-5$
Batch Size	16	8	1

F.2 Evaluation Prompts

For image captioning evaluation, we use GPT-4o-mini to determine for each image whether the predicted captions match the ground truth, with the prompt: *You are trying to tell if a candidate set of captions is describing the same image as a reference set of captions. Candidate set: {candidate_statements}. Reference set: {target_statements}. On a precise scale from 0 to 100, how likely is it that the candidate set is describing the same image as the reference set?(JSON format, with a key “score”, value between 0 and 100.*

For VQA evaluation, we use GPT-4o-mini to determine for each question whether the answers match ground truth texts, with the prompt: *Question: {question}, Ground Truth Answer: {ground_truth}, Predicted Answer: {predicted_answer}. Does the predicted answer match the ground truth? Answer 1 for match and 0 for not match. Use semantic meaning not exact match. Synonyms are also treated as a match, e.g., pond and swimming pool.*

F.3 Qualitative Results

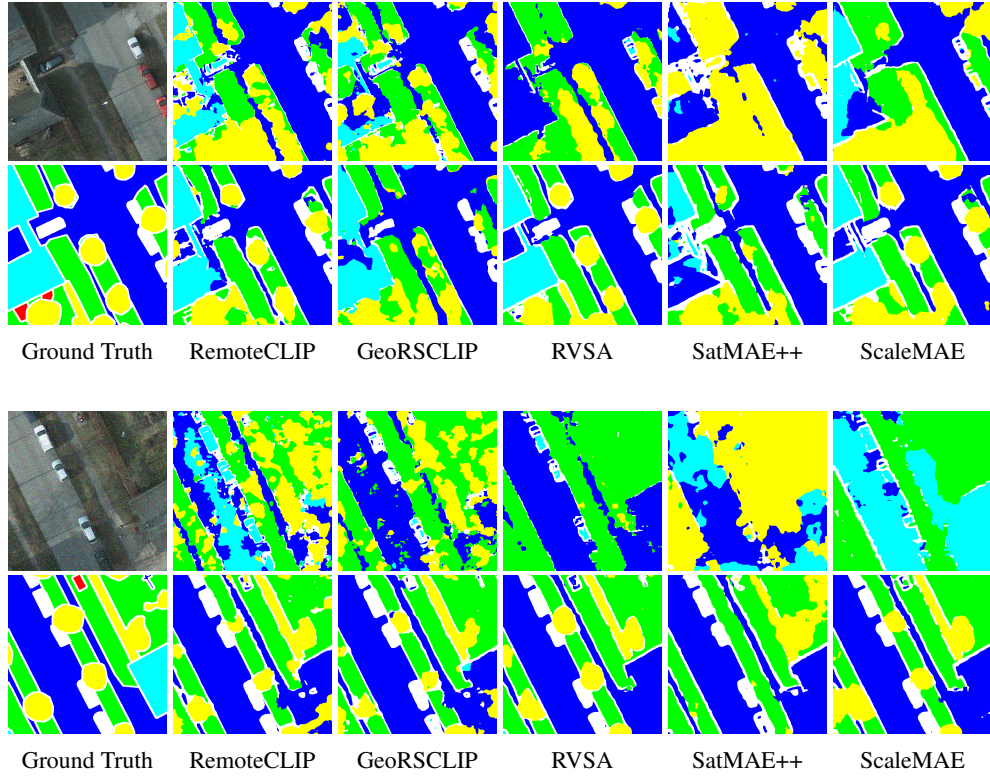


Figure 5: Selected semantic segmentation examples under (a) Gaussian noise (severity 5) and (b) Salt-and-pepper noise (severity 5). For each example, the top row shows the corrupted image and the segmentation results of different models under this corruption, and the bottom row shows the ground truth and segmentation results on clean images.

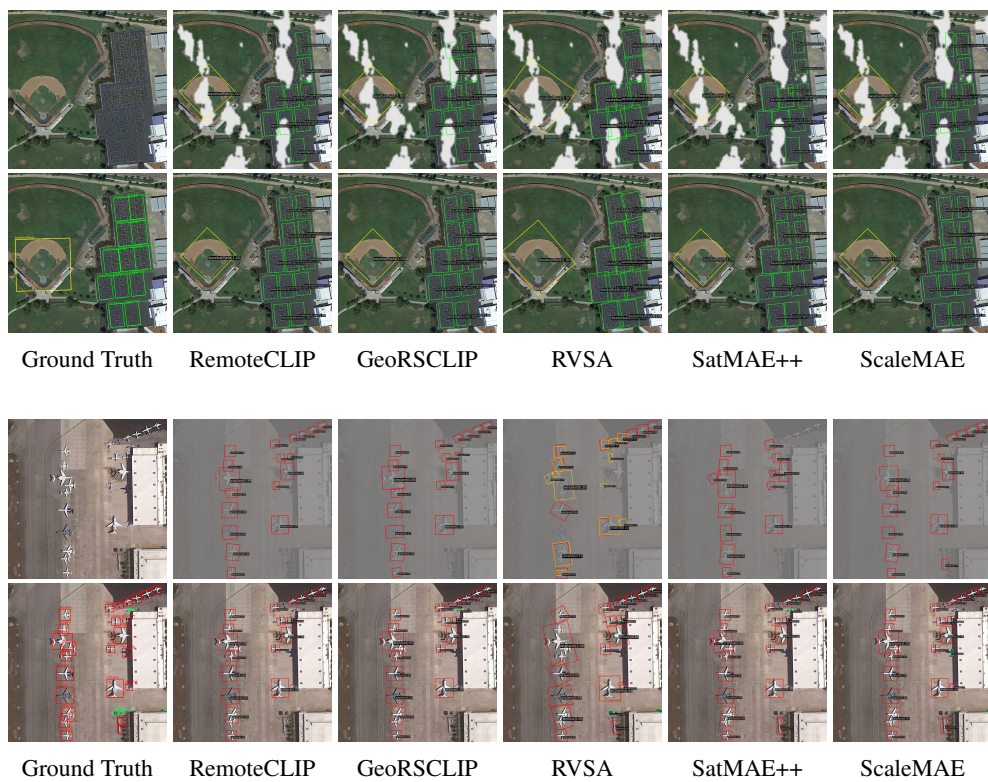


Figure 6: Selected object detection examples under (a) cloud (severity 5) and (b) brightness-and-contrast corruption (severity 5). For each example, the top row shows the corrupted image and the detection results of different models under this corruption, and the bottom row shows the ground truth and detection results on clean images.



(a)

Top image: 05925_0000.png

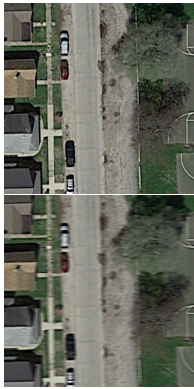
Bottom image: **Corruption type:** Data Gaps, **Severity:** 5.

GT: The image, sourced from GoogleEarth, shows a facility featuring large **storage tanks** with distinctive **white** circular structures against a **grey background**. There are **three** visible tanks, arranged from top to bottom within the frame.

RS-LLaVA: A factory features numerous **storage tanks**, with some being **white** and others having a silver appearance.

VHM: The image shows an aerial view of a large oil depot. There are **eight** large **white storage tanks** arranged in a square. Each tank has a black ring around the top. There is a road between the tanks and a white building to the left of the tanks.

Falcon: the oil tanker is equipped with **a large number** of oil tanks in the dark. yellow and white neatly placed in the oil **storage tank** on the ship. **three** large storage tanks are in a piece of bareland.



(b)

Top image: 05870_0000.png

Bottom image: **Corruption type:** Motion Blur, **Severity:** 5.

GT: Aerial view of **a residential area** from Google Earth showing a portion of a **street** with **vehicles** lined up. The capture shows **four** parked on the side of the street adjacent to houses. The **houses** have various roof colors and lawn areas.

RS-LLaVA: A **basketball court** sits on a **lawn**, surrounded by **buildings and trees**, with a **road** nearby.

VHM: The image shows a **residential area** with a **tree-lined street**. There are **houses** on **both sides** of the street. The houses are mostly made of brick and have **different colors**. The street is made of asphalt and has **cars parked** on it. There is also a basketball court on the right side of the image.

Falcon: a **road** with **two** cars and a basketball field is next to a piece of **green meadow** and **several buildings**. two cars are **running** on the wide road and there are some buildings on one side of the road.

Figure 7: Selected image captioning examples. We highlight correct information in green and incorrect information in red.



(a)

Top image: **P0003_0002.png**

Bottom image: **Corruption type:** Cloud, **Severity:** 5.

What color are the large vehicles seen in the image?

GT: Yellow, **GeoChat:** Teal, **SkySenseGPT:** teal, **VHM:** yellow.

How many small vehicles are visible in the image?

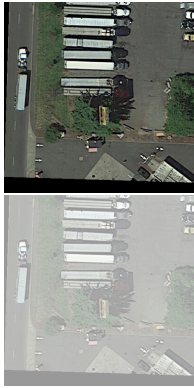
GT: 2, **GeoChat:** 11, **SkySenseGPT:** 2, **VHM:** 3.

Is there a vehicle located at the top-most position in the provided image?

GT: Yes, **GeoChat:** Yes, **SkySenseGPT:** Yes, **VHM:** no.

What is the orientation of the road in the image?

GT: North-South, **GeoChat:** Right, **SkySenseGPT:** horizontal, **VHM:** north-south.



(b)

Top image: **P0007_0004.png**

Bottom image: **Corruption type:** Haze, **Severity:** 5.

What is the predominant color of the large vehicles?

GT: white, **GeoChat:** teal, **SkySenseGPT:** white, **VHM:** white.

How are the large vehicles predominantly arranged in the parking lot?

GT: in rows, **GeoChat:** Cluster, **SkySenseGPT:** in rows, **VHM:** parked.

Are there any large vehicles that are positioned away from the main cluster?

GT: Yes, **GeoChat:** Yes, **SkySenseGPT:** Yes, **VHM:** Yes.

What is the orientation of the large vehicles in the parking lot?

GT: north-south, **GeoChat:** Vertical, **SkySenseGPT:** parallel, **VHM:** parallel.

Figure 8: Selected VQA examples. Correct answers are shown in green, and incorrect answers are shown in red.

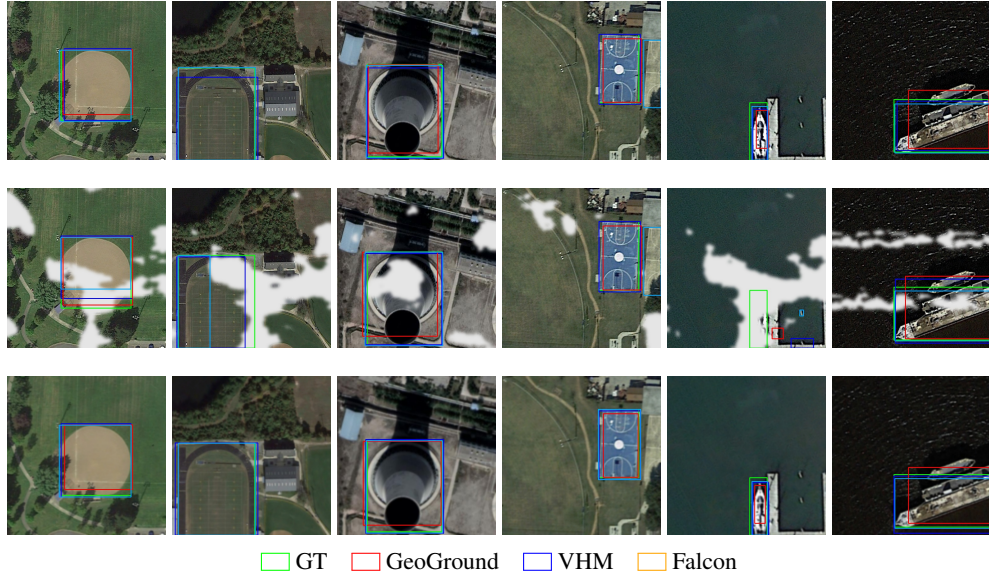


Figure 9: Selected visual grounding examples. The top row presents results on the clean images, while the second and third rows illustrate results under clouds and Gaussian blur corruptions, respectively, both applied with severity level 5. From left to right, the visual grounding questions are: “The baseball field has a brown infield and is situated in the center of the image surrounded by green grass”, “The ground track and field with multiple lanes is located next to a large building with a dark roof”, “The chimney seen in the center of the image is cylindrical and extends from the middle to the bottom of the frame”, “The basketball court featured in the image is colored in blue with white markings and is located on the right-hand side of the frame”, “The small ship is situated vertically near the bottom right corner of the image”, and “The ship positioned towards the bottom edge of the image”.